A triptych photocatalyst based on the Co-Integration of Ag nanoparticles and *carbo*-benzene dye into a TiO_2 thin film

Jérémy Cure [a,*], *Kévin Cocq* [b], *Adnen Mlayah* [a,c], *Teresa Hungria* [d], *Pierre Alphonse* [e], *Yves J. Chabal* [f], *Valérie Maraval* [b], *Remi Chauvin* [b], *Alain Estève* [a], *Carole Rossi* [a,**]

[a] *LAAS CNRS, University of Toulouse, 7 Avenue Du Colonel Roche, 31031 Toulouse, France*
[b] *LCC CNRS, University of Toulouse, 205 Route de Narbonne, 31077 Toulouse, France*
[c] *CEMES CNRS, University of Toulouse, 29 Rue Jeanne Marvig, 31055 Toulouse, France*
[d] *Centre de Microcaractérisation Raimond CASTAING, University of Toulouse, CNRS, UT3 Paul Sabatier, INP, INSA, Espace Clément Ader, 3 Rue Caroline Aigle, 31400 Toulouse, France*
[e] *CIRIMAT, University of Toulouse, CNRS, UT3 Paul Sabatier, 118 Route de Narbonne, 31062 Toulouse, France*
[f] *Department of Materials Science and Engineering, University of Texas at Dallas, Richardson, TX, USA*

HIGHLIGHTS

- TiO_2 planar photocatalyst with Ag nanoparticles and *Carbo* benzene photosensitizer.
- Design of a new efficient, long lasting and low cost triptych photocatalyst.
- Hydrogen production under ambient and pressurized conditions.
- New general technological pathway to manufacture of triptych photocatalyst.
- Original nanostructure and valuable data for benchmarking purposes are provided.

ARTICLE INFO

Keywords:
Carbo benzene dye
Silver nanoparticle
Titanium dioxide film
Triptych system
Photocatalytic hydrogen production

ABSTRACT

This work proposes a new efficient, long lasting scalable and low cost triptych photocatalyst by assembling a semiconductor thin film (planar anatase TiO_2), a photosensitive molecule of the *carbo* benzene (Cbz) family and plasmonic Ag nanoparticles with exquisite degree of intimacy with the semiconductor. Under simulated sunlight conditions over 48 h, the triptych TiO_2/Ag/Cbz photocatalyst allows a hydrogen production rate of 0.18 mmol $g^{-1}_{photocatalyst}$ h^{-1} in conditions of applicative pressure (2.2 bars) and temperature (ambient) suitable for commercial applications. A ternary synergy (~33%) for hydrogen production is clearly evidenced with the triptych material in comparison with the diptych counterpart.

The role of each component (TiO_2, Ag and Cbz) on the H_2 production is investigated systematically by discriminating the light absorption from the different materials and interfaces. We show how to achieve an efficient vertical Schottky junction between Ag

* *Corresponding author.*
** *Corresponding author.*
E mail addresses: jcure@laas.fr (J. Cure), crossi@laas.fr (C. Rossi).
https://doi.org/10.1016/j.ijhydene.2019.08.126

under pressure
Water splitting

nanoparticles and the TiO_2 substrate that is demonstrated to be of crucial importance in the water splitting process.

Introduction

Interest in hydrogen energy is greater than ever, notably because of the strong expectations for the development of new means of transport based on the improvement of fuel cell to cars, ships and even trains [1] to counterbalance the depletion of fossil fuels and global warming [2–4].

Alternately to water electrolysis and PhotoElectroCatalytic Water Splitting (PEC WS) [5–9], achieving a pure Photo Catalytic (PC) WS process from water and sunlight offers a promising approach for producing a sustainable costless and carbon free economy [10–13]. The PC WS concept is simple: sun irradiates a powdered photocatalyst dispersed in an aqueous solution and the hydrogen is readily produced [14]. Rigorously, there is no need of a counter electrode, neither of a supporting electrolyte nor a pH buffer: the photon energy is converted into electron hole pairs and then into chemical energy [15].

The PC WS concept has been validated with numerous semiconductor materials [16–18], and the majority of reports was based on Earth abundant and stable semiconductors such as titanium dioxide (TiO_2) used for its moderate redox potential *vs* SHE (e.g. $E^{\circ}_{1/2}(TiO_2/Ti^{2+})$ 0.50 V), large bandgap (Eg ~3.2 eV) and effective catalytic properties. However, the PC efficiency of semiconductors remains limited by several fac tors: (i) inability to harvest the visible light due to large band gap, only allowing the use of about 4% of the total solar radi ation while the visible light contributes to *ca* 50% of the solar irradiance, (ii) fast recombination of photo generated elec tron hole pairs before they can migrate to the surface [19,20]. Therefore, various strategies have been explored to improve the WS efficiency under solar illumination. The band gap can be narrowed and light absorption extended to longer wave lengths by doping with non metal atoms [21,22], with organic dyes [23] such as ruthenium complexes [24], porphyrins [25], or graphene oxide [26–29]. Another strategy to improve the PC efficiency relies on the use of hybrid metal nanoparticles/ semiconductor nanostructures [30–44], in order to reduce the electron hole recombination and/or to harvest the visible light owing to plasmonic enhanced optical absorption [29,30,45]. Inorganic semiconductors based on transition metal oxides, oxysulfides or oxynitrides with lower bandgap as compared to TiO_2 can also be used to increase the absorption of visible light [10–12]. Finally, the formation of heterojunctions with other semiconductors (Bi_2WO_6, m $BiVO_4$, TaON, Bi_2O_3, Ag_2O, Ag_3VO_4…) [46–51] has been proposed to induce beneficial charge separation and electronic properties in the stack.

Although significant advances have been achieved in the design of efficient materials for enhanced photocatalysis [52], the reported efficiencies are still far from those required for commercialization of operating devices.

Moreover, powdered photocatalysts, which have attracted a large attention in the past years and constitute the subject of most of the published works on PC WS, suffer from the possible dispersion of particles into the environment and are not advantageous for large scale production. Only a few concepts for scaling up these technologies have been reported [53,54]. One remarkable achievement in 2018 is the 1 m^2 flat panel reactor composed of Al doped $SrTiO_3$ powder photo catalyst, achieving a solar to hydrogen energy conversion efficiency of 0.4% by WS [15], which is still too low for large scale application of solar WS.

One challenge of solar to H_2 technology is the design of an efficient, long lasting, scalable and low cost photocatalyst, well optimized for sunlight absorption to drive catalytic hydrogen evolution, which is the scope of the present study. The originality of the presented work is to assemble a triptych material (sparse examples in the literature) and demonstrate synergistic effects between its components. This is performed within a scalable, durable and low cost (mass fabrication compatible) technological pathway, based on a planar struc ture avoiding potential dissemination of nanoparticles in the environment. The hydrogen production is measured, for the first time, under slightly over pressurized conditions, which we believe are closer to those of the device operation in envisaged applications. Results are compared to values of the literature, all recorded at the atmospheric pressure, pointing to the need of further investigation of this issue.

In more detail, we combine in an optimized assembly, a light harversting semiconductor thin film (TiO_2) with efficient and low cost noble metal (Ag) and a *carbo* benzene macro molecule to prepare a hybrid nanomaterial for H_2 generation by PC WS. For the first time, a *carbo* benzene macromolecule functionalized with two NH_2 –primary amino groups (*para* di(anilinylethynyl) tetraphenyl *carbo* benzene), hereafter denoted as Cbz is explored as photosensitizer. *Carbo* benzenes exhibit unique properties related to the "*carbo* aromatic" character of their C_{18} macrocyclic core: high π electron rich ness (~1.7 π e/C), persistent symmetry (*quasi* D_{6h}), emptiness (monocycle of *ca* 8 Å diameter) and associated residual flexi bility [55]. The physico chemical properties of the di(anilin 4 ylethynyl) derivative Cbz selected for the present study are particularly adapted to its use as a redox active photosensi tizer [56]: a structural propensity for high single molecule conductance (σ ~100 nS) [57] and a high molar extinction co efficient (ε 131 000 L mol^{-1} cm^{-1}) [55,56] at λ_{max} 493 nm complementary with the frequency of Ag NPs surface plas mon resonance (SPR) [58]. It is worth to notice here that the Cbz selected as photosensitizer in this work is, as most of other carbo benzene molecules reported to date, very weakly photoluminescent, so that the possible contribution of its emission properties can be neglected in the present study [59–63].

This triptych TiO_2/Ag/Cbz photocatalyst exhibits enhanced performances under visible light and pressure (2.2 bar) compared to those of binary TiO_2/Ag and TiO_2/Cbz systems pointing to the synergy between these three components.

Experimental methods

All chemicals are supplied by Sigma Aldrich. The glass wafers AF 32 are supplied by SCHOTT glass made of ideas®. Titania sols are prepared by hydrolysis of titanium alkoxide in a large excess of acidified water, according to the general procedure previously described [64] (see supporting informa tion, Section A).

Synthesis of TiO_2/Ag/Cbz photocatalyst

TiO_2 surface. Glass or silicon substrates are cleaned by an O_2 plasma (800 W, 5 min) prior to use. 0.5 mL of TiO_2 sol is deposited on the clean substrate by spin coating (speed: 2000 rpm, acceleration: 2000 rpm, time: 30 s). The so obtained glass/TiO_2 samples are annealed following 2 main steps: first at 110 °C for 30 min to remove the solvent and organic mole cules, then at 300 °C under air during 1 h, with a heating rate of 10 °C.min ^{1}, to stabilize the titanium oxide structure. The glass/TiO_2 samples are diced into squares (1.5 × 1.5 cm^2) and cleaned using O_2 plasma (400 W, 5 min) prior to triptych processing.

For electron microscopy observation and spectroscopic characterization, silicon/TiO_2 samples (cleaned for 5 min with O_2 plasma at 400 W) are used.

Synthesis and deposition of Ag nanoparticles on TiO_2. The Ag nanoparticles (NPs) are grown following a previously re ported procedure [65]. The TiO_2 thin film is immersed in a mixture composed by 0.5 mL of $AgNO_3$ aqueous solution ([Ag^+] 2.15 × 10 ^{3} mol/L), 0.5 mL of sodium citrate aqueous solution ([citrate] 0.05 mol/L), 4.5 mL of DI water and 0.5 mL of ethanol and irradiated under UV (100 W, 2 min). The size of the nanoparticles is fixed by the irradiation duration. The samples are then annealed in air at 200 °C during 30 min to ensure the grafting of Ag NPs into the TiO_2 film for a controlled localization of the plasmonic field close to the TiO_2/Ag interface. After annealing, the substrates are vigorously cleaned with DI water (~50 mL for each substrate) in order to remove all the by products arising from the thermal decomposition of the cit rate ligands. Some of these, hereafter labeled as TiO_2/Ag sam ples, are characterized prior to the deposition of Cbz molecules.

Synthesis and deposition of Cbz. *Para* di(anilin 4 ylethynyl)tetraphenyl *carbo* benzene, a *carbo* benzene mole cule functionalized by $-NH_2$ groups (Cbz) is synthesized by a 12 step process, according to previously described procedures [56,66]. The TiO_2/Ag substrates are immersed overnight in an anisole solution of Cbz ([Cbz] 0.05 g/L) under stirring at 50 rpm (round per minute) on a shaker platform. This final step affords the triptych TiO_2/Ag/Cbz hybrid nanomaterial depicted in Fig. 1.

Some of the triptych samples are prepared, first, by the Cbz deposition on the TiO_2 followed by the growth of the Ag NPs with the previously described procedure. Such samples are hereafter named TiO_2/Cbz/Ag.

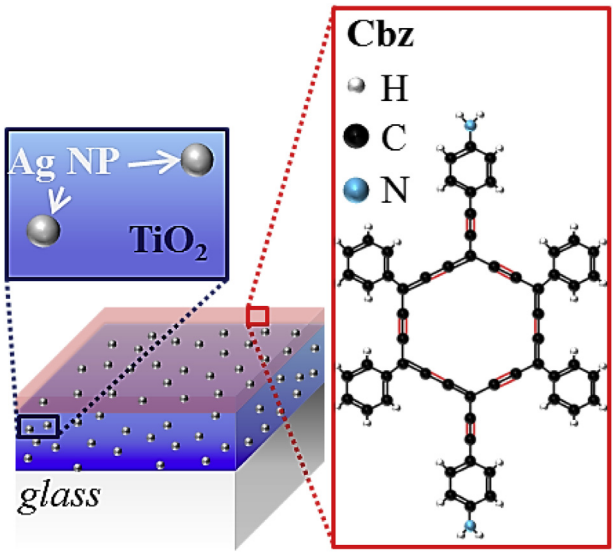

Fig. 1 – Schematic hybrid triptych nanomaterial combining a TiO_2 film (blue), Ag NPs (grey spheres) and a Cbz photosensitive layer (red). (For interpretation of the references to color in this figure legend, the reader is referred to the Web version of this article.)

Materials characterization

Structural characterization of the triptych nanomaterials are performed using Scanning Electronic Microscopy (SEM) (FEI Helios 600i Nanolab) in the immersion mode at 20 kV and with a working distance of 4.2 mm. Transmission Electronic Microscopy (TEM) and High Angle Annular Dark Field Scanning Transmission Electronic Microscopy (HAADF STEM) experiments are carried out in cross section samples prepared by Focused Ion Beam (FIB) process in a FEI Helios Nanolab. The surface of the samples is protected by a layer of sputtered carbon before the preparation of lamellas. These latter are observed on a JEM ARM200F cold FEG at 200 kV with a probe Cs corrector reaching a spatial correction of 0.078 nm. Energy Dispersive X ray Spectrom etry (EDS) spectra are recorded using a JEOL CENTURIO SDD detector. Electron Energy Loss Spectroscopy (EELS) data are acquired using a GATAN GIF QUANTUM ER using a disper sion of 0.025 eV/channel (energy resolution of 0.3 eV), a collection semi angle of 19.4 mrad and a convergence semi angle of 15 mrad. Crystalline phases are detected using Grazing Incidence X Ray Diffraction (GI –XRD, Bruker D8 Discover system) with a Cu k alpha radiation as the source. For GI XRD, the grazing angle is set to 1.2° and two theta collection angle is ranged from 20° to 80° with a step of 0.05° and a dwell time of 0.1 s per point. The absence of Ag reflections for the diptych TiO_2/Ag and triptych TiO_2/Ag/Cbz samples is presumably correlated to the low content of silver on the TiO_2 thin film and the small dimensions of the samples. Note that the GI XRD of the TiO_2 thin film pro vided in the supporting information is recorded from a whole silicon/TiO_2 wafer. The TiO_2 roughness and density are both characterized by Grazing Incidence X Ray

Reflectometry (GI XRR, Bruker D8 Discover system): the grazing angle is set to 1.2° and two theta omega collection angles is ranged from 0.4° to 3.0° with a 0.005° step and a dwell time of 0.1 s per point in all cases. X ray photoelec tron spectroscopy (XPS) (ESCALAB 250 X Ray photoelectron spectrometer) with a monochromatized Al Kα radiation, a concentric hemispherical electron energy analyzer under vacuum (10 ^{9} mbar) and a pass energy of 23.5 eV is used to characterize the chemical species at the interfaces of the triptych nanomaterial. The Raman scattering spectra are acquired using a Horiba Jobin Yvon XPlora set up. The spectra are excited by a 532 nm laser beam focused onto the sample using a 100× objectives (0.8 NA). The laser power intensity is kept as low as 0.1 mW in order to avoid sample heating and degradation of the organic Cbz layer. The absorbance spectra are recorded in the transmission mode from the triptych nanomaterials deposited on the trans parent glass substrates using a PerkinElmer Lambda 950 UV–vis spectrometer equipped with an integration sphere (specular mode). The hydrophobicity of the Cbz layer is characterized by drop contact angle measurements using a Digidrop system. For each sample, three successive mea surements are performed in order to check the reproduc ibility and estimate a mean value of the contact angle. Inductively coupled plasma optical emission spectrometry (ICP OES) measurements are performed at the "Service d'analyse élémentaire" of LCC CNRS in Toulouse using a Thermo Scientific iCAP 6300 DUO spectrometer with a 3 channel, 12 roller pump and a 27.12 MHz solid state RF plasma generator. Typically, all the 10 mL (aqueous solu tion) involved in the photocatalytic experiments are evap orated overnight in a 50 mL Teflon tube. Concentrated nitric acid is added in the resulting mixture and then diluted in a 10 mL volumetric flask. The resulting solution (5 mL) is introduced during the ICP OES analysis. Note that the cali bration curve are realized by successive dilution of a 1000 ppm standard to give a series of standards with values at: 0.5; 1; 2; 5; 10 and 20 ppm. Each standard is analyzed in 3 replicates. The values of the working wavelength are 328.068 and 338.289 nm.

Measurement of photocatalytic activity

Lab made quartz reactors are used to characterize the pho tocatalytic properties of the prepared samples (Fig. S1). The hydrogen production is measured by gas chromatography (GC, PerkinElmer Clarus 580, thermal conductivity detector, PlotQ column (30 m) and PE molisieve column (30 m), argon carrier gas). The samples (1.5 cm × 1.5 cm, 2.25 cm^2) are immersed into a 65:35 deionized water:ethanol mixture (10 mL). The quartz reactor is purged and pressurized at 2.2 bar under argon gas in order to remove the air. The samples are then irradiated with a Xenon lamp supplied by Cermax® (elliptical PE300B–10F, UV–visible, 300 W, wavelengths range from 300 nm to 1100 nm, sample placed at a distance of ~12 cm which corresponds to an optical irradiance at the sample of 28 mW cm ^{2}) during 48 h and the quantity of exhausted hydrogen is measured every 6 h. For each sample, several characterization are made to ensure reproducibility of the measurements. The relative spectral distribution of the Xenon lamp is presented in Fig. S2.

Results

Structural and chemical characterization of the triptych material

Fig. 2 gives optical (a) and SEM (b) images and a TEM cross section view (c) of a TiO_2/Ag/Cbz sample on silicon showing a uniform and dense Ag NP deposition, which are covered by a 6 nm thick layer of Cbz. A closer examination shows that the Ag NPs (mean size: 7 ± 2 nm, areal NP density: 349 ± 10 NPs/μm^2) have grown not only on the TiO_2 surface but also in the grain interstices of the TiO_2 film, as revealed by the STEM EDS chemical profile (Fig. 2d). Silver nanocrystals exhibit typical (111) crystallographic planes (blue frame in Fig. 2c) [67]. The thickness, density and roughness of the TiO_2 film are esti mated by GI XRR at ~80 nm, 2.9 ± 0.01 g cm ^{3}, well below the bulk density of 3.89 g cm ^{3} and ~2 ± 0.1 nm, respectively [68]. The anatase single phase and the stoichiometry of the TiO_2 film are confirmed by the XRD patterns and XPS analysis, respectively. The latter gives the binding energies of the Ti $2p_{1/2}$, Ti $2p_{3/2}$ and O 1s core levels at 464.5 ± 0.1 eV, 458.8 ± 0.1 eV and 530.0 ± 0.1 eV, respectively (see supporting information, Section B 1) [69].

The Cbz layer is visible (Fig. 2c) as the well defined black contrast on top of the Ag NPs; the grey region on top of the Cbz layer is attributed to the carbon layer used to prepare the FIB lamella. EELS analyses of this top layer (Fig. 2e) shows a shift from 24.3 eV to 22.4 eV in the carbon plasmon (σ + π) peak energy across the C Cbz interfacial region. Laffont *et al.* re ported a correlation between the plasmon (σ + π) energy E_p and the physical properties (resistivity, Young's modulus and thermal conductivity) of carbon species, i.e. a correlation be tween a shift of E_p and the nature of the carbon material [70]. Similarly, Longo *et al.* reported a shift of E_p from 33 to 28 eV when comparing diamond carbon and amorphous carbon [71,72]. As shown in Fig. 2e, both the contrast and shift of the C EELS peak reveal the information of a ~6 nm thick Cbz layer covering the entire surface of the Ag NPs.

The Raman spectra of the triptych TiO_2/Ag/Cbz nano material measured in the 400 4000 cm ^{1} range are presented in Fig. 3a. Sharp peaks are clearly observed in this spectral range owing to the Surface Enhanced Raman Scattering (SERS) effect produced by the Ag NPs. Indeed, SERS effect is here observable because the Raman excitation line (532 nm) is close to the surface plasmon resonances of the aggregated Ag NPs. As a matter of fact, the Raman spectra measured from the TiO_2/Cbz substrate, i.e. without any Ag NP, reveal almost no Raman signal (black trace, Fig. 3a) [73,74].

It is worth mentioning that the weak signal/noise ratio of the SERS spectra shown in Fig. 3a (red trace) is due to the fact that the Raman scattering was excited with a minimum laser power (0.1 mW) to avoid degradation of the Cbz layer which occurs at higher power because of heating resulting from the optical absorption by the Cbz and in the Ag NPs.

By comparison of these Raman spectra with the infrared spectra of Cbz and analogous *para* dianilinyltetraphenyl

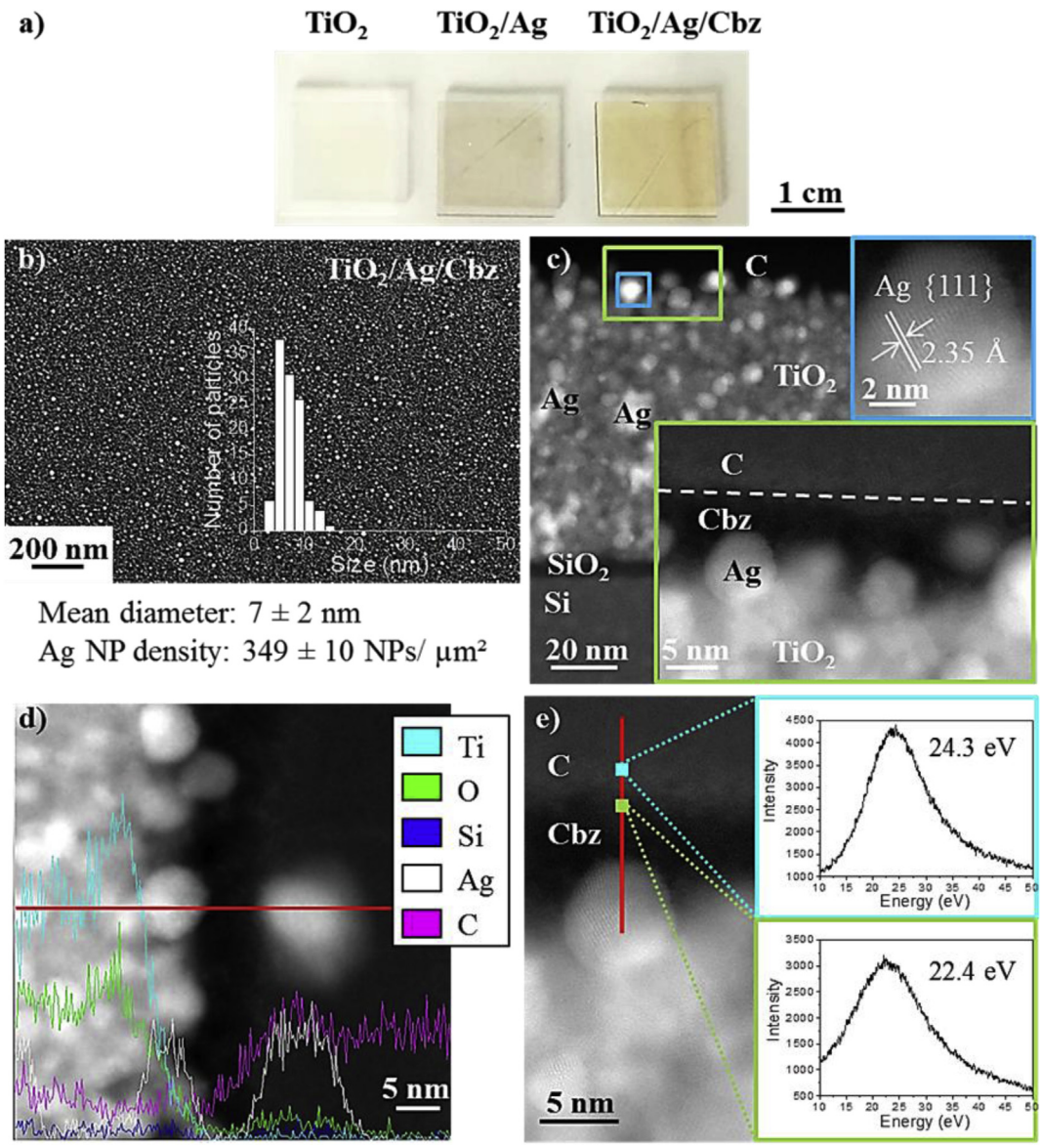

Fig. 2 – a) Optical images and b) SEM observation (inset of the size distribution of Ag NPs onto the TiO_2 surface) of the TiO_2/Ag/Cbz material; c) HAADF-STEM cross-section images of TiO_2/Ag/Cbz coated with a thin sputtered carbon layer (inset of magnified images, green and blue frames); d) HAADF-STEM image and EDS spectra obtained along the red line; e) HAADF-STEM and EELS spectra: plasmon spectra from the protective carbon layer (blue square and frame) and from the Cbz layer (green square and frame). Dotted lines are eye guides. (For interpretation of the references to color in this figure legend, the reader is referred to the Web version of this article.)

carbo benzene without *exo* macrocyclic C≡C spacers, named Cbz* (Fig. S5), the main sharp modes can be unambiguously assigned to –N(–H)$_2$ (3250 and 3053 cm ^{1}), C≡C (2149 cm ^{1} and 2037 cm ^{1}) and aromatic C=C (1580 and 1511 cm ^{1}) stretching modes. According to a combined experimental and density functional theory (DFT) computational study of the Raman spectra of a series of *carbo* benzenes [75], the two bands at 2149 cm ^{1} and 2037 cm ^{1} can be assigned to the coupled vibrations of the *exo* and *endo* macrocyclic C≡C bonds together. The most intense one, at 2037 cm ^{1}, corre sponds to the asymmetric mode, the other (at 2149 cm ^{1}) corresponding to the superimposition of the in phase and out of phase modes of the *exo* C≡C bonds with respect to the totally symmetric vibration of the *endo* C≡C bonds [75].

Remarkably, the intensity of band at 2149 cm ^{1} is much weaker than that at 2037 cm ^{1} when the Cbz layer is formed directly on the TiO_2 surface, which suggests a selective enhancement of SERS intensity of both the *exo* and *endo* macrocyclic C≡C modes in the TiO_2/Ag/Cbz nanomaterial (Fig. S6). Moreover, the enhancement of the Raman intensity of the C≡C and of the NH_2 modes in the triptych nanomaterial, indicates that the anilin 4 ylethynyl functions are localized in the close vicinity of the Ag NPs [73,74], which suggests that the Cbz molecules are bound to the Ag NPs by the NH_2 groups.

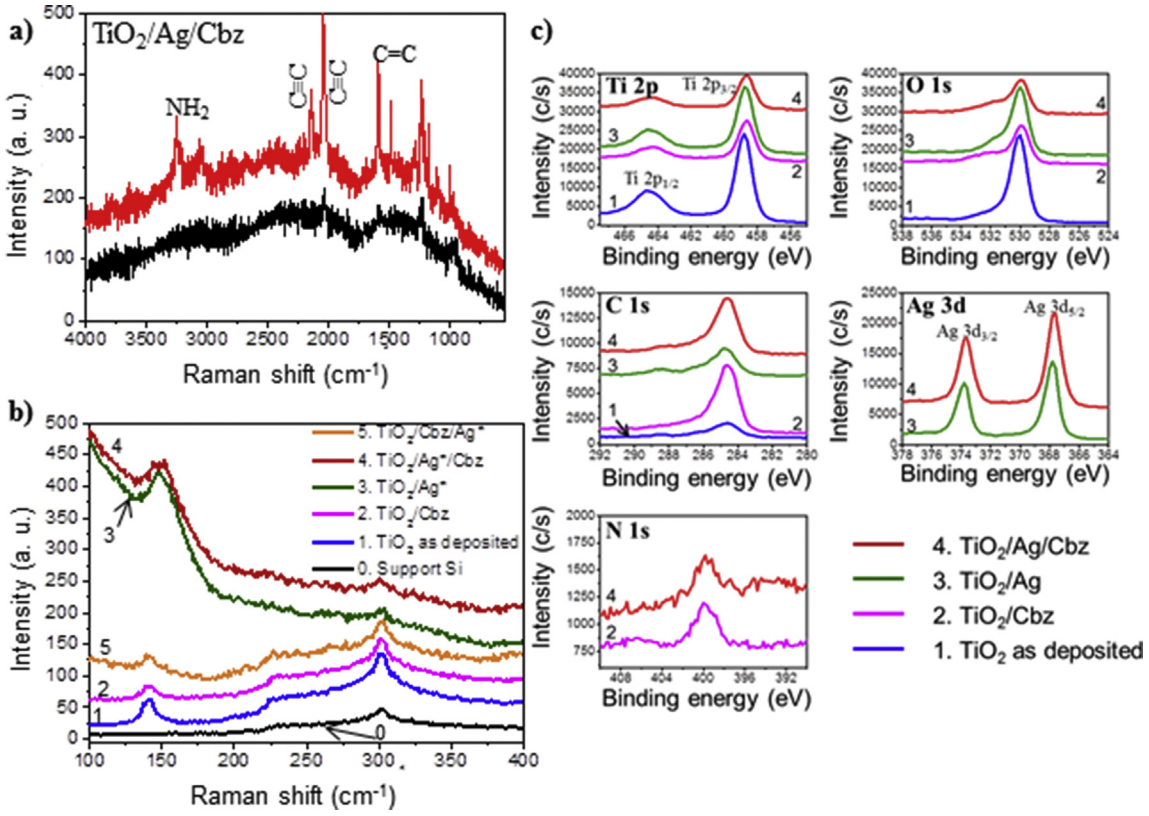

Fig. 3 – a) Raman spectra of TiO_2/Ag/Cbz in the 4000-400 cm ^{1} range recorded on a single Ag aggregate (red top curve) and away from the aggregate (black bottom curve); the size of the aggregate is comparable to the laser spot size (1 μm^2); b) Raman spectra recorded in the 400-100 cm ^{1} range for the Si reference substrate (0, black), TiO_2 thin film as deposited (1, blue), TiO_2/Cbz (2, violet), TiO_2/Ag* (3, dark green), TiO_2/Ag*/Cbz (4, dark red) and TiO_2/Cbz/Ag* material (5, dark orange) in the case of larger Ag NPs; c) XPS spectra of TiO_2 thin film (1, blue), TiO_2/Cbz (2, violet), TiO_2/Ag (3, green) and TiO_2/Ag/Cbz (4, red) for the Ti $2p_{3/2,1/2}$; O 1s; C 1s; Ag $3d_{5/2,3/2}$; and N 1s regions. Dotted lines are eye guides. (For interpretation of the references to color in this figure legend, the reader is referred to the Web version of this article.)

Raman spectroscopy also reveals microstructure features, as well as the presence of electronic interactions in the diptych TiO_2/Ag and triptych TiO_2/Ag/Cbz materials. By increasing the time of the Ag NP growth, these phenomena are even more evident in the TiO_2/Ag* series with larger Ag NPs (Fig. 3b, see supporting information, Section B 3) compared to the TiO_2/Ag series (see supporting information, Section B 4). The low frequency (100 400 cm ^{1}) Raman spectra (Fig. 3b) exhibit a peak characteristic of the E_g1 phonon mode of anatase TiO_2: it is located at 140 cm ^{1} in TiO_2, at 147 cm ^{1} in both TiO_2/Ag* and TiO_2/Ag*/Cbz (Fig. 3b) and at 140 cm ^{1} again in the reversed triptych TiO_2/Cbz/Ag*, without TiO_2/Ag interface.

Moreover, the intensity of the TiO_2 Raman peak is clearly enhanced in TiO_2/Ag and TiO_2/Ag/Cbz with respect to TiO_2 and TiO_2/Cbz/Ag. This clearly shows that the blue shift and the intensity of the TiO_2 Raman peak correlate with the for mation of the TiO_2/Ag interface. The observation of such a blue shift has already been reported in TiO_2/Au films and was attributed to the deposition of Au NPs preferably on oxygen vacancies and edge sites which favors the charge transfer interactions between TiO_2 and metal nanoparticles [13]. The charge transfer phenomenon may also enhance the photo catalytic activity since the photo generated electron hole pairs could be spatially separated and hence their lifetime significantly increased [76]. The blue shifted Raman peak of the TiO_2 phonon also means that the Ti–O bond is stronger at the TiO_2/Ag interface than in bulk TiO_2, revealing a charge transfer from the metal nanoparticle to the semiconductor. Moreover, the blue shift of the *Eg*1 phonon mode can also result from the mechanical constraints applied in the TiO_2 network, confirming the complete filling of the TiO_2 pores by larger Ag NPs as discussed above. These interactions are ex pected since the annealing step performed after NP growth, should increase the intimacy and accommodate a transition between both TiO_2 and Ag crystalline networks. Note that no significant shift is observed in the Raman spectra when the Cbz is deposited on TiO_2, pointing to the non destructive in teractions between the TiO_2 and the Cbz (violet trace, Fig. 3b).

Additionally, XPS spectra given in Fig. 3c clearly show an increase of the intensity of C 1s peaks and a decrease of the intensity of Ti 2p and O 1s peaks for the diptych TiO_2/Cbz and triptych TiO_2/Ag/Cbz nanomaterials which is expected when the Cbz layer covers the top surface (see supporting infor mation, Section B 5). Finally, XPS spectra also show that N 1s core level (from –NH_2 groups) is exactly at the same position (399.8 eV) than for TiO_2/Cbz which suggests a similar binding between Cbz and TiO_2 and the Ag NP surfaces (Fig. 3c, see supporting information, Section B 5). Note that some carbon

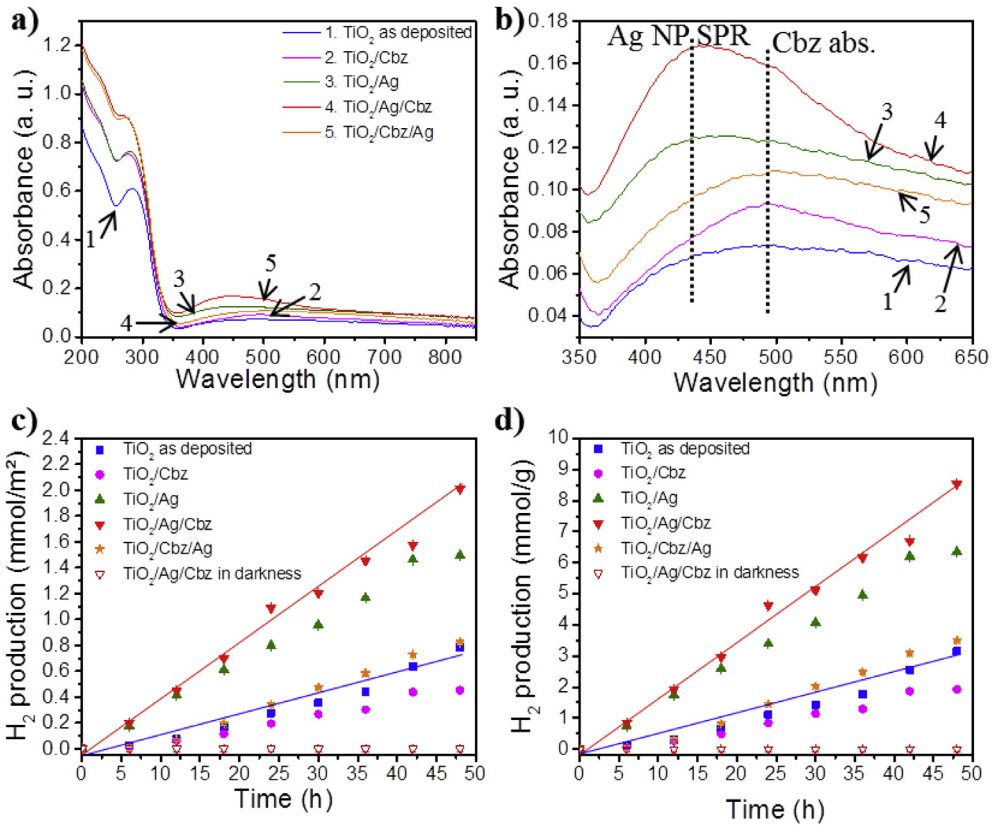

Fig. 4 – a) UV–visible spectra (in transmission) in the 200–850 nm region and; b) in the 350–650 nm region; c) H_2 production per surface units and; d) per mass units for pure ~80 nm TiO_2 thin film (1, blue, square), TiO_2/Cbz (2, violet, circle), TiO_2/Ag (3, green, triangle), TiO_2/Ag/Cbz (4, red, reverse triangle) and TiO_2/Cbz/Ag (5, orange, star) on glass substrates (1.5 × 1.5 cm) immersed into a 65:35 deionized water:ethanol solution at room temperature and pressurized under argon at 2.2 bar. Error scale bars of hydrogen quantity are added for each plot. Note that the monitoring of the H_2 production in darkness is for the triptych TiO_2/Ag/Cbz material (red, empty reverse triangle) in the same conditions: deionized 65:35 water:ethanol solution at room temperature under argon at 2.2 bar. (For interpretation of the references to color in this figure legend, the reader is referred to the Web version of this article.)

contamination coming from atmospheric adsorbed carbon species is detected on a few samples (without a coating of Cbz) with a C 1s peak of weak intensity (Fig. 3c).

UV–visible spectroscopy and hydrogen production of the diptych and triptych nanomaterials

The optical absorption spectra of the investigated samples are presented in Fig. 4a and b. The contribution of each compo nent of the diptych and triptych nanomaterials can be clearly distinguished: (i) the strong band gap absorption of TiO_2 is observed around 280 nm; (ii) the contribution of the Ag NPs SPR is visible around 430 nm in both TiO_2/Ag and TiO_2/Ag/Cbz compared to pure TiO_2 and is consistent with the SPR wave length expected for spherical 7 ± 2 nm Ag NPs [39,40]; (iii) the main absorption band of Cbz molecules resulting from the overlapping of the two strongest Gouterman transitions (HOMO 1/HOMO → LUMO/LUMO+1) appears around 494 nm as a shoulder in the TiO_2/Ag/Cbz spectrum and is probably enhanced by the SPR of the Ag NPs [59,60,77,78]. Note that in the reversed triptych system TiO_2/Cbz/Ag, the Ag NPs are no longer in direct contact with the TiO_2 surface, which affects their LSPR properties by red shifting and broadening [79], resulting in an overlap of the Ag NPs LSPR peak with the ab sorption band of Cbz, leading to the observation of only one broad absorption band (Fig. 4b). From these UV–visible ana lyses, the band gap of the TiO_2 thin films has been calculated for the different diptych and triptych systems and are found both close to ~3.4 eV (Fig. S14).

The H_2 production is measured by immersing the 2.25 cm^2 samples into 10 mL of a 35% aqueous ethanol solution in a hand made quartz reactor. Importantly, the reactor is purged and pressurized with 2.2 bar of argon gas before analyses and is not placed under vacuum as it is the case in many literature reports [11,80]. A sample of bare TiO_2 thin film is also studied as a reference.

The hydrogen production of all tested samples (Fig. 4c and d) increases linearly during the two days tests and reveals a stable catalytic performance during 48 h. The measured hydrogen production rates are determined: 0.03 mmol m^{-2} h^{-1} (0.13 mmol g^{-1} h^{-1}) and 0.04 mmol m^{-2} h^{-1} (0.18 mmol g^{-1} h^{-1}) for the diptych TiO_2/Ag and triptych TiO_2/Ag/Cbz nanomaterials, respectively. These rates exceed by more than a factor 2 those of the TiO_2 reference layer:

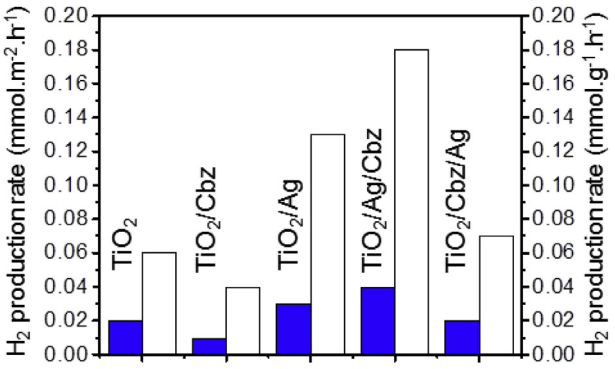

Fig. 5 – The H_2 production rate per surface units (blue) and per gram (white) for the tested photocatalysts. (For interpretation of the references to color in this figure legend, the reader is referred to the Web version of this article.)

0.02 mmol m ^{2} h ^{1} (0.06 mmol g ^{1} h ^{1}), of the TiO_2/Cbz: 0.009 mmol m ^{2} h ^{1} (0.04 mmol g ^{1} h ^{1}) and of the reversed triptych TiO_2/Cbz/Ag nanomaterial: 0.02 mmol m ^{2} h ^{1} (0.07 mmol g ^{1} h ^{1}), hence underlying the synergetic role of the TiO_2/Ag in the PC process (Fig. 4c and d, Fig. 5). Moreover, the production rate of the triptych TiO_2/Ag/Cbz is larger than that of the diptych TiO_2/Ag by ~33% which gives an estimate of the contribution of the Cbz photo sensitizer to the photo catalytic process.

The extension of the TiO_2/Ag/Cbz triptych absorption over a large visible range (from 400 to 600 nm) as compared to TiO_2 alone may lead to a more efficient utilization of the visible light and thus enhance the hydrogen production. Further more, because the absorptions of Ag NPs (SPR) and Cbz (maximum absorption band) take place at two different wavelengths, their combination can also induce the observed enhancement of the photocatalytic efficiency.

Discussion

Influence of the respective spatial distribution of the three components

To better assess the respective role of the Cbz organic dye and plasmonic Ag NPs into the TiO_2/Ag/Cbz nanomaterial, three different samples are assembled: (1) a sample without the organic dye: TiO_2/Ag; (2) a sample without Ag NPs: TiO_2/Cbz; (3) a sample where the Cbz layer is deposited before the growth of the Ag NPs i.e. preventing the contact between the TiO_2 pores and the environing medium: the reversed triptych: TiO_2/Cbz/Ag. In the latter sample, no shift of the phonon mode E_g1 is measured (Fig. 3b, Fig. S10) indicating the absence of mechanical constraint on the TiO_2 lattice, as expected: the Cbz layer indeed covers the surface of the TiO_2 film and avoid the embedding of Ag NPs in the pores of the metal oxide film.

The samples are placed under Ar flow and irradiated in the presence of ethanol in the same conditions as those used for the TiO_2/Ag/Cbz nanomaterial. In all the cases, the hydrogen production increases linearly over the 48 h (Fig. 4c and d). The hydrogen production rate for each sample is represented in Fig. 5. As expected, the TiO_2/Ag substrate is more efficient than the pure TiO_2 thin film due to SPR effects, but the hydrogen production rate of this diptych is lower than that of the TiO_2/Ag/Cbz triptych.

The diptych TiO_2/Ag nanomaterial is 1.9 times more effi cient than pure TiO_2 if the H_2 production rate is expressed per m^{2} (0.03 mmol m ^{2} h ^{1}), and 2.2 times more efficient (0.13 mmol g ^{1} h ^{1}), if this rate is expressed per gram. For the TiO_2/Ag/Cbz triptych, a slight improvement of the production rate is observed, up to 2 times (0.04 mmol m ^{2} h ^{1}), or up to 3 times more (0.18 mmol g ^{1} h ^{1}) than pure TiO_2 depending on the considered unit (Fig. 5). In contrast, the decreased efficiency observed for the TiO_2/Cbz diptych clearly evi dences a synergistic effect between the three components in the TiO_2/Ag/Cbz triptych.

Additionally, the stability of the TiO_2/Ag/Cbz triptych is tested by cyclic photocatalytic H_2 production monitoring (Fig. 6). After 5 cycles, no significant decay in the photo catalytic activity is observed, suggesting that TiO_2/Ag/Cbz have good stability in photocatalytic H_2 production under harsh environment: simulated sunlight illumination (optical irradiance at the sample of 28 mW cm ^{2}), room temperature and pressure (2.2 bar). The optical and SEM observations of the samples after the photocatalytic experiments show a better stability of the TiO_2/Ag/Cbz triptych compared to the TiO_2/Ag diptych on which the photoactive film is highly degraded (Fig. S17). These observations reveal that the Cbz layer also acts as a protective layer against the TiO_2 photocorrosion [81,82].

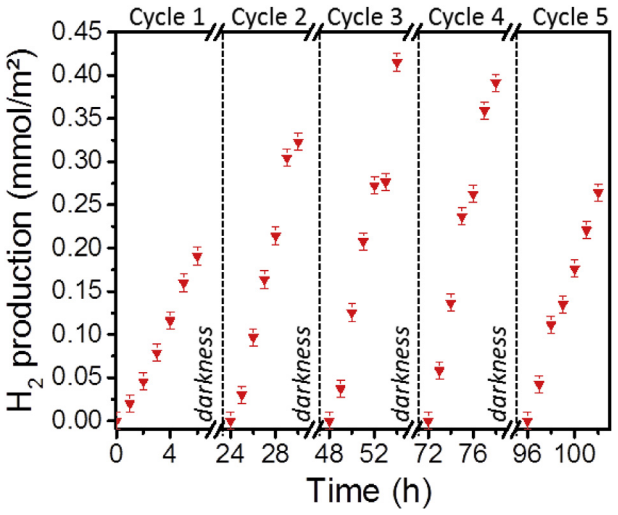

Fig. 6 – Cyclability of TiO_2/Ag/Cbz triptych in H_2 production under visible light irradiation. Cumulated evolution of hydrogen from a triptych sample (1 × 1 cm) immersed into a 65:35 deionized water:ethanol solution at room temperature and pressurized under argon at 2.2 bar. Error scale bars of hydrogen quantity are added for each plot. Note that each cycle is realized over 6 h after a period of 18 h into darkness (i.e. the sample remains immersed into the deionized 65:35 water:ethanol solution under pressure of argon (2.2 bar) and at room temperature during the 18 h of darkness).

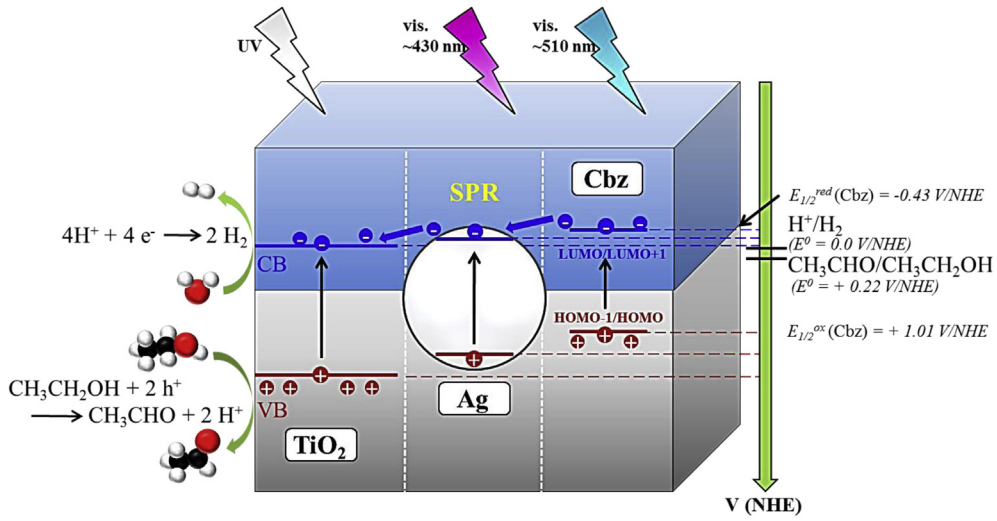

Fig. 7 – Illustration of a possible electron transfer mechanism in the triptych TiO_2/Ag/Cbz material. The semiconductor thin film (TiO_2), the photosensitive Cbz layer and Ag nanoparticle are depicted as grey, blue and white, respectively. Note that for each component of the triptych, the band diagram is also depicted. (For interpretation of the references to color in this figure legend, the reader is referred to the Web version of this article.)

This remarkable enhancement of the hydrogen production rate observed with TiO_2/Ag/Cbz and to a lesser extent with TiO_2/Ag is attributed to the Ag metal link in the effective vertical Schottky junction between Ag NPs and TiO_2. The plasmon mode corresponds to discrete states (interbands 4d – 5s) of coupling between the incident light and the electronic density oscillation within the Ag NPs. The energy of the photon is transferred to electrons which can get over the Shottky barrier at the interface between TiO_2 and Ag and be injected into the conduction band of TiO_2. This mechanism called plasmon induced electron transfer from metallic par ticles to a TiO_2 film is schematically represented in Fig. 7. Importantly, the surface plasmon resonance of the Ag NPs spectral domain is overlapping with the optical absorption of the Cbz molecules, the latter giving a shoulder of the Ag NPs LSPR broad band (Fig. 4b): this leads to a plasmonic enhance ment of the photo generation of electrons and holes and might explain the synergy observed in the hydrogen produc tion with the triptych nanomaterials.

The lower hydrogen production activity of the reversed TiO_2/Cbz/Ag triptych, close to the TiO_2/Cbz level, can be tentatively explained by two effects. Ag NPs absorb light, but without the metal link between Ag and TiO_2, hot elec trons cannot be transferred into the TiO_2 thus preventing the enhancement of hydrogen production. Nevertheless the energy is transferred to the Cbz dye which contributes to slightly increase the hydrogen production as compared to TiO_2/Cbz [83], and thus probably because of the electron transport ability of the Cbz molecule [57]. The poor perfor mance of the latter sample as compared to pure TiO_2 could be attributed to the hydrophobicity of the Cbz layer, hampering the interaction between the TiO_2 surface and water molecules.

Indeed, the contact angles systematically increases when the Cbz layer is deposited on the samples as compared to those measured for the same materials without organic layer (see supporting information, Section B 8). For example, the contact angle of 62 ± 3° of the TiO_2/Ag diptych increases up to 100.2 ± 0.1° after deposition of the Cbz layer. The fact that the triptych system, despite the screening of charge in addition to the physico chemical separation of water molecules from the catalytic surface sites, which is clearly visible from the diptych response, is a clear illustration of the synergy between Ag nanoparticles and Cbz molecules. With this respect, a better control of the Cbz layer thickness, as well as its organization at the molecular level, to facilitate water diffusion, is a potential source of enhancement of the triptych material performances.

All these observations clearly evidence the synergetic ef fect of the three components in the triptych materials and highlight the key role of electron transfer mechanisms for the H_2 production as illustrated in Fig. 7.

Influence of the Ag loading and size

As the Ag–TiO_2 metal link was shown to play a crucial role in the hydrogen production performances of the TiO_2/Ag/Cbz nanomaterial, this last section addresses the effect of loading and size of Ag NPs. The porosity of the TiO_2 films allows nucleation and growth of Ag NPs inside the pores, from molecular precursors such as $AgNO_3$, which has a larger van der Waals size than water or ethanol molecules. The size of Ag NPs can be easily tuned by modifying the time of irradiation inducing the process of photo deposition of Ag NPs from their salt precursor. Typically, the length ening of the UV irradiation time for the photo reduction process from 2 to 30 min induces an increase of the size of the Ag NPs in the corresponding TiO_2/Ag* series. Two populations of Ag NPs are observed after a 30 min illumi nation: well defined small particles with an average diam eter of 18 ± 6 nm and larger ones with an average diameter of 30 ± 2 nm, the areal density being almost constant at ~344 ± 10 NPs/μm^2 (see supporting information, Section B 3). Inside the pores of the TiO_2 film, the Ag NPs growth is

limited by the volume of the pores, thus leading to the first population of smaller Ag NPs (18 ± 6 nm), while the larger NPs (30 ± 2 nm) are those located at the TiO_2 film surface where their growth is not limited by any confinement. The smaller Ag NPs are thus the result of the growth inside the pores, whereas the bigger particles are those which grew on the TiO_2 surface.

The TiO_2/Ag* diptych produces much less hydrogen than TiO_2/Ag: 0.004 mmol m ^{2} h ^{1} (0.02 mmol g ^{1} h ^{1}) and 0.03 mmol m ^{2} h ^{1} (0.13 mmol g ^{1} h ^{1}), respectively (see supporting information, Section B 7). Three explanations can be proposed: (1) the aggregation of Ag NPs decreases the number and the accessibility of the active sites on the surface of the triptych material; (2) a too large covering of the surface by silver can shield the UV light absorption by the TiO_2, and thus decrease the utilizing efficiency of pho toelectrons [84]; (3) the reduction of free TiO_2 surface accessible to water molecules since the pores are filled with ~18 nm plasmonic particles (Fig. S9). The SPR effect of 18 nm Ag NPs completely embedded into the TiO_2 pores is characterized at ~380 nm (see supporting information, Fig. S13) [85]. The maximum of the SPR absorption band resulting from the contribution of two Ag NP populations onto the surface (18 ± 6 nm and 30 ± 2 nm, Fig. S8b) in TiO_2/Ag* remains at ~430 nm, i.e. roughly at the same position as for ~7 nm Ag NPs obtained after a 2 min irradiation process. In the dual population case, we believe the largely pre dominant population (18 nm) to be responsible for the non shifted TiO_2/Ag* result (no shifting expected for NPs with diameter < ~20 nm), the population with larger diameter being minor, with a contribution also vanishing due to the broadening of the overall absorption peak. So, the size of the Ag NPs has apparently no effect on the efficiency of the water reduction photocatalyst. However, a higher loading of NPs appears to be critical on the photocatalyst perfor mances since it reduces the TiO_2 effective surface area in the final material.

Comparison with already published catalytic materials

Finally, the main characteristic and PC WS performances of our TiO_2/Ag/Cbz photocatalyst are reported in Table 1, together with other triptych materials (mostly in nanopowder form) described in the recent literature [52,86–89]. Note that the comparison is difficult because the experimental param eters are highly variable. We characterize the H_2 production under 2.2 bar representative of practical applications whereas a major part of published works [11,80] measure the photo catalytic activity in a quartz reactor under vacuum, which is highly favorable to hydrogen production because of the shift of the chemical equilibrium according to the Le Chatelier's principle: 2 H_2O 2 H_2 + O_2. Nevertheless, our TiO_2/Ag/Cbz photocatalyst thin film exhibits very good PC WS perfor mance (180 μmol g ^{1} h ^{1}) under high pressure (2.2 bar). In addition, compared to other works, the manufacturing pro cess is not only low costs but also provides robust material against photocorrosion compared to nanopowders (estab lished over 48 h (see supporting information, Fig. S17 and Section B 13)).

Table 1 – PC performance of different type of triptych photocatalysts under visible light irradiation.

Material		Surface area	Solution composition	Light intensity (mW/cm^2)	Light source (Spectrum light source)	H_2 production rate (μmol.g^{-1}.h^{-1})	Pressure (bar)	Cost	Robustness	Reference
nanopowder	Au@r-GO/TiO2	122 9 m^2 g^{-1}	'5% H^2,O 25% MeOH	100 mW cm^{-2}	Xenon light source (λ >400 nm)	300 μmol-g^{-1} h^{-1}	1 bar	$$$	–	[86]
nanopowder	Au/TiO_2-gC_3N_4	75 m^2 g^{-1}	99%H_2O 1% MeOH	12 5 mW cm^{-2}	150-W metal halide lamp (λ all spectrum)	580 μmol g^{-1} h^{-1}	–	$$$	–	[52]
nanopowder	Ag–TiO_2-graphene	–	80% H_2O 20% MeOH	450 1 mW cm^{-2}	300-W Xenon lamp (λ all spectrum)	130 μmol g^{-1} h^{-1}	1 bar	$$	–	[87]
nanosheet	TiO_2–Pt-rGO	334 7 m^2 g^{-1}	90% H_2O 10% MeOH	–	300-W Xenon lamp (λ all spectrum)	4000 μmol g^{-1} h^{-1}	1 bar	$$	–	[89]
nortosheet	TiO_2–Ag-rGO	70 83 m^2 g^{-1}	80% H_2O 20% MeOH	–	280-W Xenon lamp (λ- all spectrum)	593 (μmol g^{-1} h^{-1}	–	$$	–	[88]
hin film	TiO_2/Ag/Cbz	4 25 m^2 g^{-1}(*)	65% H_2O 35% EtOH	28 mW cm^{-2}	300-W Xenon lamp (λ 300–1100 nm)	180 μmol g^{-1} h^{-1} 40 μmol m^{-2} h^{-1}	2 2 bar	$	✓✓✓	This work

*)Note that the surface area of TiO_2/Ag/Cbz is calculated from the dimension and mass of the thin film since the surface area is too weak to be measured by Brunauer-Emmett-Teller (BET) method

Conclusion

In summary, the innovative TiO_2/Ag/Cbz triptych system with an ultralow weight of photocatalyst, which is of paramount importance in the perspective of low cost applications in the field of energy, benefits from synergy effect for hydrogen production by pure photocatalysis as shown by comparison with the diptych systems. The relevance of triptych materials for WS involving a semiconductor thin film, a plasmonic nanoparticle and a specific photosensitive molecule of the *carbo* benzene genus is established. Thanks to an adapted procedure of photo deposition, the pores of a TiO_2 thin film can be metallized by silver nanoparticles in one step. The present work not only demonstrates the high interest of *carbo* benzene molecules in green hydrogen production applica tions, but also provides a mechanistic insight highlighting two key requirements: the need for a Schottky junction between silver and TiO_2 and the precise localization of the dye in triptych materials in order to promote a synergic effect for H_2 production by hydrogen evolution reaction.

Furthermore, although thin films based systems are typi cally used in photoelectrochemical processes for hydrogen production, the improvement of thin films efficiency by their combination with adequate materials like plasmonic nano particles and/or photosensitive and innovative molecules was demonstrated, allowing their use in pure photocatalytic con ditions i.e. without any need of electric energy to produce hydrogen from water and sunlight, and more importantly under usual conditions of ambient temperature and pressure.

Author contributions

J. C. prepared all the materials, performed all the H_2 produc tion measurements and directed and supervised the research. K. C. performed the synthesis of the photosensitive *carbo* benzene molecule. A. M. provided support for Raman experi ments. All HAADF STEM and TEM images were obtained by T. H. . P. A. provided the titania sol. C. T. performed XRD mea surements. Y. J. C. provided support for XPS data analysis. V. M. and R. C. provided support for the synthesis of *carbo* ben zene molecules. A. E. provided support for manuscript prep aration. C. R. directed and supervised the research with J. C. .

Acknowledgement

All the synthesis and spectroscopic characterization and modeling were supported by ANR and the Université de Tou louse (IDEX MUSE project). This work was supported by LAAS CNRS technology platform, a member of Renatech network. Jean François Veyan is acknowledged for his help in the measurements of the XPS spectra. The authors thank Claudie Josse and Armel Descamps Mandine (Centre de Micro caractérisations Raimond Castaing) for the preparation of lamelas and HAADF STEM observations, Alain Moreau for the ICP measurements and Andréa Nicollet and Séverine Vivies for their help with XRD characterization. Tercio de Freitas Paulo is deeply acknowledged for his help in the assigment of the Raman spectra.

Appendix A. Supplementary data

Supplementary data to this article can be found online at https://doi.org/10.1016/j.ijhydene.2019.08.126.

REFERENCES

[1] 10th stakeholder forum fuel cell and hydrogen technology: Europe's journey to a greener world. Publications Office of the European Union; 2017.
[2] Dutta S. A review on production, storage of hydrogen and its utilization as an energy resource. J Ind Eng Chem 2014;20(4):1148 56.
[3] ADEME. The role of hydrogen in the energy transition, technical review. 2018. p. 1 15.
[4] Pinaud BA, Benck JD, Seitz LC, Forman AJ, Chen Z, Deutsch TG, James BD, Baum KN, Baum GN, Ardo S, Wang H, Miller E, Jaramillo TF. Technical and economic feasibility of centralized facilities for solar hydrogen production via photocatalysis and photoelectrochemistry. Energy Environ Sci 2013;6(7):1983 2002.
[5] Abdi FF, Han L, Smets AHM, zeman M, Dam B, Van De Krol R. Efficient solar water splitting by enhanced charge separation in a bismuth vanadate silicon tandem photoelectrode. Nat Commun 2013;4:2195.
[6] Luo J, Vermaas DA, Bi D, Hagfeldt A, Smith WA, Grätzel M. Bipolar membrane assisted solar water splitting in optimal pH. Adv Energy Mater. 2016;6(13):1600100.
[7] Ager JW, Shaner M, Walczak K, Sharp ID, Ardo S. Experimental demonstrations of spontaneous, solar driven photoelectrochemical water splitting. Energy Environ Sci 2015;8(10):2811 24.
[8] Prevot MS, Guijarro N, Sivula K. Enhancing the performance of a robust sol gel processed p type delafossite CuFeO2 photocathode for solar water reduction. ChemSusChem 2015;8(8):1359 67.
[9] Fujishima A, Honda K. Electrochemical photolysis of water at a semiconductor electrode. Nature 1972;238(5358):37 8.
[10] Hisatomi T, Kubota J, Domen K. Recent advances in semiconductors for photocatalytic and photoelectrochemical water splitting. Chem Soc Rev 2014;43(17):7520 35.
[11] Wang Z, Li C, Domen K. Recent developments in heterogeneous photocatalysts for solar driven overall water splitting. Chem Soc Rev 2018;48(7):2109 25.
[12] Maeda K, Teramura K, Lu D, Takata T, Saito N, Inoue Y, Domen K. Photocatalyst releasing hydrogen from water. Nature 2006;440(7082):295.
[13] Melvin AA, Illath K, Das T, Raja T, Bhattacharyya S, Gopinath CS. M Au/TiO2 (M = Ag, Pd, and Pt) nanophotocatalyst for overall solar water splitting: role of interfaces. Nanoscale 2015;7(32):13477 88.
[14] Wang X, Jin S, An H, Wang X, Feng Z, Li C. Relation between the photocatalytic and photoelectrocatalytic performance for the particulate semiconductor based photoconversion systems with surface phase junction structure. J Phys Chem C 2015;119(39):22460 4.
[15] Goto Y, Hisatomi T, Wang Q, Higashi T, Ishikiriyama K, Maeda T, Sakata Y, Okunaka S, Tokudome H, Katayama M, Akiyama S, Nishiyama H, Inoue Y, Takewaki T, Setoyama T, Minegishi T, Takata T, Yamada T, Domen K. A particulate

photocatalyst water splitting panel for large scale solar hydrogen generation. Joule 2018;2(3):509 20.
[16] Kudo A, Miseki Y. Heterogeneous photocatalyst materials for water splitting. Chem Soc Rev 2009;38(1):253 78.
[17] Osterloh FE. Inorganic materials as catalysts for photochemical splitting of water. Chem Mater 2008;20(1):35 54.
[18] Chen XB, Shen SH, Guo LJ, Mao SS. Semiconductor based photocatalytic hydrogen generation. Chem Rev 2010;110(11):6503 70.
[19] Tian Y, Tatsuma T. Mechanisms and applications of plasmon induced charge separation at TiO2 films loaded with gold nanoparticles. J Am Chem Soc 2005;127(20):7632 7.
[20] Takai A, Kamat PV. Capture, store, and discharge. Shuttling photogenerated electrons across TiO2 silver interface. ACS Nano 2011;5(9):7369 76.
[21] Khan SUM, Al Shahry M, Ingler WB. Efficient photochemical water splitting by a chemically modified n TiO2 2. Science 2002;297(5590):2243 5.
[22] Varley JB, Janotti A, Van de Walle CG. Mechanism of visible light photocatalysis in nitrogen doped TiO2. Adv Mater 2011;23(20):2343 +.
[23] Rojas HC, Bellani S, Sarduy EA, Fumagalli F, Mayer MT, Schreier M, Grätzel M, Di Fonzo F, Antognazza MR. All solution processed, hybrid organic inorganic photocathode for hydrogen evolution. ACS Omega 2017;2(7):3424 31.
[24] Reisner E, Powell DJ, Cavazza C, Fontecilla Camps JC, Armstrong FA. Visible light driven H2 production by hydrogenases atteched to dye sensitized TiO2 nanoparticles. J Am Chem Soc 2009;131(51):18457 66.
[25] Watanabe M, Sun S, Ishihara T, Kamimura T, Nishimura M, Tani F. Visible light driven dye sensitized photocatalytic hydrogen production by porphyrin and its cyclic dimer and trimer: effect of multi pyridyl anchoring groups on photocatalytic activity and stability. ACS Appl Energy Mater 2018;1(11):6072 81.
[26] Zhang X, Sun Y, Cui X, Jiang Z. A green and facile synthesis of TiO2/graphene nanocomposites and their photocatalytic activity for hydrogen evolution. Int J Hydrogen Energy 2012;37(1):811 5.
[27] Huang Q, Tian S, Zeng D, wang X, Song W, Li Y, Xiao W, Xie C. Enhanced photocatalytic activity of chemically bonded TiO2/graphene composites based on the effective interfacial charge transfer through the C Ti bond. ACS Catal 2013;3(7):1477 85.
[28] Putri LK, Tan LL, Ong WJ, Chang WS, Chai SP. Graphene oxide: exploiting its unique properties toward visible light driven photocatalysis. Appl Mater Today 2016;4:9 16.
[29] Min S, Lu G. Dye cosensitized graphene/Pt photocatalyst for high efficient visible light hydrogen evolution. Int J Hydrogen Energy 2012;37(14):10564 74.
[30] Liu EZ, Kang LM, Yang YH, Sun T, Hu XY, Zhu CJ, Liu HC, Wang QP, Li XH, Fan J. Plasmonic Ag deposited TiO2 nano sheet film for enhanced photocatalytic hydrogen production by water splitting. Nanotechnology 2014;25(16):165401.
[31] Yin YC, Liu EZ, Li H, Wan J, Fan J, Hu XY, Li J, Tang CN, Pu CC. Fabrication of plasmonic Au/TiO2 nanotube arrays with enhanced photoelectrocatalytic activities. Ceram Int 2016;42(8):9387 95.
[32] Liu Y, Yang S, Zhang S, Wang H, Yu H, Cao Y, Peng F. Design of cocatalyst loading position for photocatalytic water splitting into hydrogen in electrolyte solutions. Int J Hydrogen Energy 2018;43(11):5551 60.
[33] Bai S, Yang L, Wang C, Lin Y, Lu J, Jiang J, Xiong Y. Boosting photocatalytic water splitting: interfacial charge polarization in atomically controlled core shell cocatalysts. Angew Chem Int Ed 2015;54:14810 4.
[34] Liu J, Liu G, Li M, Shen W, Liu Z, Wang J, Zhao J, Jiang L, Song Y. Enhancement of photochemical hydrogen evolution over Pt loaded hierarchical titania photonic crystal. Energy Environ Sci 2010;3(10):1503 6.
[35] Fraters BD, Amrollahi R, Mul G. How Pt nanoparticles affect TiO2 induced gas phase photocatalytic oxidation reactions. J Catal 2015;324:119 26.
[36] Zhang Z, Zhang L, Hedhili MN, Zhang H, Wang P. Plasmonic gold nanocrystals coupled with photonic crystal seamlessly on TiO2 nanotube photoelectrodes for efficient visible light photoelectrochemical water splitting. Nano Lett 2013;13(1):14 20.
[37] Pu Y C, Wang G, Chang K D, Ling Y, Lin Y K, Fitzmorris BC, Liu C M, Lu X, Tong Y, Zhang JZ, Hsu Y J, Li Y. Au nanostructure decorated TiO2 nanowires exhibiting photoactivity across entire UV visible region for photoelectrochemical water splitting. Nano Lett 2013;13(8):3817 23.
[38] Gao H, Zhang P, Zhao J, Zhang Y, Hu J, Shao G. Plasmon enhancement on photocatalytic hydrogen production over the Z scheme photosynthetic heterojunction system. Appl Catal B 2017;210:297 305.
[39] Ge M Z, Cao C Y, Li S H, Tang Y X, Wang L N, Qi N, Huang J Y, Zhang K Q, Al Deyab SS, Lai Y K. In situ plasmonic Ag nanoparticle anchored TiO2 nanotube arrays as visible light driven photocatalysts for enhanced water splitting. Nanoscale 2016;8(9):5226 34.
[40] Sreedhar A, Sreekanth TVM, Kwon JH, Yi J, Sohn Y, Gwag JS. Ag nanoparticles decorated ion beam assisted TiO2 thin films for tuning the water splitting activity from UV to visible light harvesting. Ceram Int 2017;43(15):12814 21.
[41] Chaudhary P, Ingole PP. Multifunctional plasmonic Ag hematite nano dendrite electrocatalysts for methanol assisted water splitting: synergism between silver nanoparticles and hematite dendrites. Int J Hydrogen Energy 2018;43(3):1344 54.
[42] Arunachalam P, Amer MS, Ghanem MA, Al Mayouf AM, Zhao D. Activation effect of silver nanoparticles on the photoelectrochemical performance of mesoporous TiO2 nanospheres photoanodes for water oxidation reaction. Int J Hydrogen Energy 2017;42(16):11346 55.
[43] Amin MA, Fadlallah SA, Alosaimi GS. In situ aqueous synthesis of silver nanoparticles supported on titanium as active electrocatalyst for the hydrogen evolution reaction. Int J Hydrogen Energy 2014;39(34):19519 40.
[44] Amin MA, Fadlallah SA, Alosaimi GS, Kandemirli F, Saracoglu M, Szunerits S, Boukherroub R. Cathodic activation of titanium supported gold nanoparticles: an efficient and stable electrocatalyst for the hydrogen evolution reaction 2016;41(15):6326 41.
[45] Zhou L, Swearer DF, Zhang C, Robatjazi H, Zhao H, Henderson L, Dong L, Christopher P, Carter EA, Nordlander P, Halas NJ. Quantifying hot carrier and thermal contributions in plasmonic photocatalysis. Science 2018;362(6410):69 72.
[46] Wang JX, Huang J, Xie HL, Qu AL. Synthesis of g C3N4/TiO2 with enhanced photocatalytic activity for H 2 evolution by a simple method. Int J Hydrogen Energy 2014;39(12):6354 63.
[47] Ong W J, Tan L L, Ng YH, yong S T, Chai S P. Graphitic carbon nitride (g C3N4) based photocatalysts for artificial photosynthesis and environmental remediation: are we a step closer to achieving sustainability? Chem Rev 2016;116(12):7159 329.
[48] Chai B, Peng T, Mao J, Li K, Zan L. Graphitic carbon nitride (g C3N4) Pt TiO2 nanocomposite as an efficient photocatalyst for hydrogen production under visible light irradiation. Phys Chem Chem Phys 2012;14(48):16745 52.

[49] Yan HJ, Yang HX. TiO2 g C3N4 composite materials for photocatalytic H2 evolution under visible light irradiation. J Alloy Comp 2011;509(4):L26 9.
[50] Luo Q, Zhang L, Chen XF, Tan OK, Leong KC. Mechanochemically synthesized m BiVO4 nanoparticles for visible light photocatalysis. RSC Adv 2016;6:15796 802.
[51] Zhang L, Luo Q, Chen X, Tse MS, Tan OK, Li KHH, Tay YY, Lim CK, Guo X, Leong KC. Mechanochemically synthesized CuO/m BiVO4 composite with enhanced photoelectrochemical and photocatalytic properties. RSC Adv 2016;6:65038 46.
[52] Marchal C, Cottineau T, Mendez Medrano MG, Colbeau Justin C, Caps V, Keller V. Au/TiO2 gC3N4 nanocomposites for enhanced photocatalytic H2 production from water under visible light irradiation with very low quantities of sacrificial agents. Adv Energy Mater 2018;8(14):1702142.
[53] Turan B, Becker JP, Urbain F, Finger F, Rau U, Haas S. Upscalling of integrated photoelectrochemical water splitting devices to large areas. Nat Commun 2016;7:12681.
[54] Schröder M, Kailasam K, Borgmeyer J, Neumann M, Thomas A, Schomäcker R, Schwarze M. Hydrogen evolution reaction in a large scale reactor using a carbon nitride photocatalyst under natural sunlight irradiation. Energy Technol 2015;3(10):1014 7.
[55] Cocq K, Lepetit C, Maraval V, Chauvin R. Carbo aromaticity and novel carbo aromatic compounds. Chem Soc Rev 2015;44(18):6535 59.
[56] Cocq K, Barthes C, Rives A, Maraval V, Chauvin R. Synthesis of functional carbo benzenes with functional properties: the C2 tether key. Synlett 2019;30(1):30 43.
[57] Li Z, Borguet E, Smeu M, Ratner MA, Rives A, Maraval V, Chauvin R. Towards graphyne molecular electronics. Nat Commun 2015;6:6321.
[58] Alenzi N, Liao W S, Cremer PS, Sanchez Torres V, Wood TK, Ehlig Economides C, Cheng Z. Photoelectrochemical hydrogen production from water/methanol decomposition using Ag/TiO2 nanocomposite thin films. Int J Hydrogen Energy 2010;35(21):11768 75.
[59] Baglai I, de Anda Villa M, Barba Barba RM, Poidevin C, Ramos Ortiz G, Maraval V, Lepetit C, Saffron Merceron N, Maldonado J L, Chauvin R. Difluorenyl carbo benzenes, hydrocarbon quadrupolar chromophores: synthesis, electronic structure, and two photon absorption properties. Chem Eur J 2015;21:14186 95.
[60] Listunov D, Duhayon C, Poater A, Mazères S, Saquet A, Maraval V, Chauvin R. Steric/n electronic insulation of the carbo benzene ring: dramatic effect of tert butyl vs phenyl crowns on geometric, chromophoric, redox and magnetic properties. Chem Eur J 2018;24:10699 710.
[61] Rives A, Baglai I, Malytskyi V, Maraval V, Saffron Merceron N, Voitenko Z, Chauvin R. Highly π electron rich macro aromatics: bis(p aminophenyl) *carbo* benzenes and their DBA acyclic references. Chem Commun 2012;48:8763 5.
[62] Baglai I, Maraval V, Voitenko Z, Volovenko Y, Chauvin R. Towards fluorescent indolyl *carbo* benzenes. Fr Ukr J Chem 2013;1:48 53.
[63] Barthes C, Zhu C, Khodzhaieva R, Maraval V, Chauvin R, Roshal A. Spectral properties of Expanded π systems: light absorption and emission of a tetraphenyl *carbo* benzene, manuscript in preparation. In: presented as a poster in: Book of the 10th international Chemistry Conference Toulouse kiev (ICTK 10), Toulouse, June 3 5, 2019, Poster no P53; 2019. in preparation.
[64] Alphonse P, Varghese A, Tendero C. Stable hydrosols for TiO2 coatings. J Sol Gel Sci Technol 2010;56:250 63.
[65] Cure J, Assi H, Cocq K, Marin L, Fajerwerg K, Fau P, Beche E, Chabal YJ, Esteve A, Rossi C. Controlled growth and grafting of high density Au nanoparticles on zinc oxide thin films by photo deposition. Langmuir 2018;34(5):1932 40.
[66] Leroyer L, Zou C, Maraval V, Chauvin R. Synthesis and stereochemical resolution of a [6]pericyclynedione: versatile access to pericyclynediol precursors of carbo benzenes. Compt Rendus Chem 2009;12(3 4):412 29.
[67] Cure J, Coppel Y, Dammak T, Fazzini PF, Mlayah A, Chaudret B, Fau P. Monitoring the coordination of amine ligands on silver nanoparticles using NMR and SERS. Langmuir 2015;31(4):1362 7.
[68] Horn M, Schwerdtfeger CF, Meagher EP. Z Krist 1972;136:273 81.
[69] Agarwala S, Ho GW. Synthesis and tuning of ordering and cristallinity of mesoporous titanium dioxide film. Mater Lett 2009;63(18 19):1624 7.
[70] Laffont L, Monthioux M, Serin V. Plasmon as tool for in situ evaluation of physical properties for carbon materials. Carbon 2002;40(5):767 80.
[71] Longo P, Twesten RD, Olivier J. Probing the chemical structure in diamond based materials using combined low loss and core loss electron energy loss spectroscopy. Microsc Microanal 2014;20(3):779 83.
[72] Reznik B, Fotouhi M, Gerthsen D. Structural analysis of pyrolytic carbon deposits on a planar cordierite substrate. Carbon 2004;42(7):1311 3.
[73] Persson BNJ. On the theory of surface enhanced Raman scattering. Chem Phys Lett 1981;82(3):561 5.
[74] Romero I, Aizpurua J, Bryant Garnett W, Garcia De Abajo FJ. Plasmons in nearly touching metallic nanoparticles: singular response in the limit of touching dimers. Opt Express 2006;14(21):9988 99.
[75] T. de Freitas Paulo, V. Bernardes Génisson, V. Maraval, R. Chauvin, manuscript in preparation (2019).
[76] Seh ZW, Liu S, Low M, Zhang S Y, Liu Z, Mlayah A, Han M Y. Janus Au TiO2 photocatalysts with strong localization of plasmonic near fields for efficient visible light hydrogen generation. Adv Mater 2012;24(17):2310 4.
[77] Leroyer L, Lepetit C, Rives A, Maraval V, Saffon Merceron N, Kandaskalov D, Kieffer D, Chauvin R. From hexaoxy [6] pericyclines to carbo cyclohexadienes, carbo benzenes, and dihydro carbo benzenes: synthesis, structure, chromophoric and redox properties, Chem. Eur J 2012;18:3226 40.
[78] Zhu C, Poater A, Duhayon C, Kauffmann B, Saquet A, Maraval V, Chauvin R. Carbo biphenyls and carbo terphenyls: oligo(phenylene ethynylene) ring carbo mer. Angew Chem Int Ed 2018;57:5640 4.
[79] Roldan MV, Pellegri NS, de Sanctis OA. Optical response of silver nanoparticles stabilized by amines to LSPR based sensors. Procedia Materials Science 2012;I:594 600.
[80] Takata T, Domen K. Particulate photocatalysts for water splitting: recent advances and future prospects. ACS Energy Lett 2019;4(2):542 9.
[81] Das C, Ananthoju B, Dhara AK, Aslam M, Sarkar SK, Balasubramaniam KR. Electron selective TiO2/CVD graphene layers for photocorrosion inhibition in Cu2O photocathodes. Adv Mater Interfaces 2017;4(17). n/a.
[82] Tang Y, Hu X, Liu C. Perfect Inhibition of CdS photocorrosion by graphene sheltering engineering on TiO2 nanotube array for highly stable photocatalytic activity. Phys Chem Chem Phys 2014;16(46):25321 9.
[83] Andrei C, Lestini E, Crosbie S, de Frein C, O'Reilly T, Zerulla D. Plasmonic enhancement of dye sensitized solar cells via a tailored size distribution of chemically functionalized gold nanoparticles. PLoS One 2014;9(10):e109836/1 109836/12.
[84] Yang Z, Zhang P, Ding Y, Jiang Y, Long Z, Dai W. Facile synthesis of Ag/ZnO heterostructures assisted by UV irradiation: highly photocatalytic property and anhanced photostability. Mater Res Bull 2011;46(10):1625 31.

[85] Cushing SK, Li J, Bright J, Yost BT, Zheng P, Bristow AD, Wu N. Controlling plasmon induced resonance energy transfer and hot electron injection processes in metal@TiO2 core shell nanoparticles. J Phys Chem C 2015;119(28):16239 44.
[86] Wang M, Han J, Xiong H, Guo R. Yolk@Shell nanoarchitecture of Au@r GO/TiO2 hybrids as powerful visible light photocatalysts. Langmuir 2015;31(22):6220 8.
[87] Sheu F J, Cho C P. Investigation of the appropriate content of graphene in Ag TiO2 graphene ternary nanocomposites applied as photocatalysts. Int J Hydrogen Energy 2017;42(27):17020 9.
[88] Wang Z, Low Z X, Zeng X, Su B, Yin Y, Sun C, Williams T, Wang H, Zhang X. Vertically heterostructured TiO2 Ag rGO ternary nanocomposite constructed with {001} facetted TiO2 nanosheets for enhanced Pt free hydrogen production. Int J Hydrogen Energy 2017;43(3):1508 15.
[89] Wong TJ, Lim FJ, Gao MM, Lee GH, Ho GW. Photocatalytic H2 production of composite one dimensional TiO2 nanostructures of different morphological structures and crystal phases with graphene. Catal Sci Technol 2013;3(4):1086 93.